Journal of Materials Chemistry A

Selective Synthesis of Monodispersed Bimetallic Nickel-Cobalt Phosphates with Different Nanoarchitectures for Battery-Like Supercapacitors

Journal:	*Journal of Materials Chemistry A*
Manuscript ID	TA-ART-10-2023-006584.R1
Article Type:	Paper
Date Submitted by the Author:	17-Mar-2024
Complete List of Authors:	Septiani, Ni Luh Wulan; National Research and Innovation Agency Republic of Indonesia, Research Center for Advanced Materials; Institut Teknologi Bandung, Advanced Functional Materials Research Group Kaneti, Yusuf; The University of Queensland, Bioengineering and Nanotechnology Chowdhury, Silvia ; The University of Queensland Australian Institute for Bioengineering and Nanotechnology, ; The University of Queensland Hardiansyah, Andri; National Research and Innovation Agency Republic of Indonesia Rinawati, Mia; National Taiwan University of Science and Technology, Department of Chemical Engineering Yeh, Min-Hsin; National Taiwan University of Science and Technology, Department of Chemical Engineering NARA, Hiroki; National Institute for Materials Science, International Center for Materials Nanoarchitectonics Yamauchi, Yusuke; University of Queensland, Chemical Engineering; The University of Queensland Australian Institute for Bioengineering and Nanotechnology, Yuliarto, Brian; Institut Teknologi Bandung, Engineering Physics

Selective Synthesis of Monodispersed Bimetallic Nickel-Cobalt Phosphates with Different Nanoarchitectures for Battery-Like Supercapacitors

Ni Luh Wulan Septiani[a, b†], Silvia Chowdhury[c], Andri Hardiansyah[a], Mia Rinawati[d], Min-Hsin Yeh[d], Hiroki Nara[e*], Yusuke Yamauchi[c, f, g], Yusuf Valentino Kaneti[c*], Brian Yuliarto[b, h*]

[a] *Research Center for Nanotechnology Systems, National Research and Innovation Agency (BRIN), Kawasan Puspiptek, Serpong, South Tangerang 15314, Indonesia*

[b] *Advanced Functional Materials Laboratory, Department of Engineering Physics, Institute of Technology Bandung (ITB), Bandung 40132, Indonesia*

[c] *Australian Institute for Bioengineering and Nanotechnology (AIBN), The University of Queensland, Brisbane, QLD 4072, Australia*

[d] *Department of Chemical Engineering, National Taiwan University of Science and Technology, Taipei 10607, Taiwan*

[e] *International Center for Materials Nanoarchitectonics (WPI-MANA), National Institute for Materials Science (NIMS), 1-1 Namiki, Tsukuba, Ibaraki 305-0044, Japan*

[f] *Department of Materials Process Engineering Graduate School of Engineering, Nagoya University, Nagoya, 464-8603, Japan*

[g] *Department of Plant and Environmental New Resources, Kyung Hee University, 1732 Deogyeong-daero, Giheung-gu, Yongin-si, Gyeonggi-do, 446-01 South Korea*

[h] *Research Center for Nanosciences and Nanotechnology (RCNN), Institute of Technology Bandung (ITB), Bandung 40132, Indonesia*

E-mails: v.kaneti@uq.edu.au; nara.hiroki@nims.go.jp; brian@itb.ac.id

Abstract

This work reports the fabrication of monodisperse nickel-cobalt phosphate particles with varying structures *via* the solvothermal reaction of nickel-cobalt glycerate spheres with triethyl phosphate (TEP) in different solvents followed by subsequent calcination in air at 600 °C. The choice of solvent affects the morphology of the resulting nickel-cobalt phosphate precursor obtained from the solvothermal reaction. It is found that alcohol-based solvents (pure ethanol and ethanol/butanol mixture) favour the formation of monodisperse plate-like particles, while the use of a water/ethanol mixture promotes the generation of rod-like particles. The optimized amorphous nickel-cobalt phosphate sample prepared using pure ethanol followed by calcination in air at 600 °C (E-NiCo-TEP-600) exhibits a battery-like behaviour with a high specific capacity of 620 C g^{-1} (specific capacitance of 1550 F g^{-1}) in 6.0 M KOH at a current density of 2 A g^{-1}. Furthermore, the asymmetric supercapacitor (ASC) fabricated using E-NiCo-TEP-600 as the cathode and commercial activated carbon (AC) as the anode (E-NiCo-TEP-600//AC ASC) displays a maximum energy density of 45 Wh kg^{-1} at a power density of 750 W kg^{-1}. The stability test reveals the good long-term stability of this ASC with a high capacitance retention of ~100% after 5000 cycles at a high current density of 10 A g^{-1}. The porous nature along with the high structural disorder and rich mesopores in the amorphous nickel-cobalt phosphate plate-like particles (E-NiCo-TEP-600) can promote faster diffusion of electrolyte ions and better electrolyte ion penetration, leading to a higher electrochemical performance. These results indicate the promising potential of porous amorphous bimetallic phosphate particles for supercapacitors.

Keywords: Transition metal phosphates; Two-dimensional; Supercapacitors; Asymmetric supercapacitors; Energy storage

1. Introduction

Currently, fossil fuels account for approximately 80% of the global energy production. The increasing industrialization and the growth in global population have led to an increase of energy demand which cannot be met by fossil fuels alone. This is largely due to the current shortage and unrenewable nature of fossil fuels. Furthermore, the burning of fossil fuels releases significant emissions of carbon dioxide (CO_2) into the air which causes air pollution and climate change. Hence, significant efforts have been made renewable energy resources, including biomass, wind, solar, hydropower, and geothermal to address the energy scarcity and reduce the carbon footprint.[1-3] However, these energy sources currently account only for ~ 20% of the world's total energy due to their intermittent nature.[4] Therefore, it is necessary to invest in energy storage devices to meet the increasing global energy demand.

The storing of energy can be realized using energy storage devices, such as fuel cells, flywheel, thermal energy storages, batteries, and supercapacitors.[5] Among them, electrochemical capacitors or supercapacitors have attracted significant interest as a promising alternative to lithium-ion batteries (LIBs) especially in applications requiring high power density and fast charge-discharge are required.[2, 6] There are three types of supercapacitors, electrostatic double layer capacitance (EDLC), pseudocapacitors, and battery-like supercapacitors (often termed as 'supercapattery'). Battery-like supercapacitors combines the high energy density of batteries and the high power density of supercapacitors.[3, 7-9] In addition, they offer the additional advantages, such as better safety, environmentally friendly, long lifetime, and ease of fabrication. In battery-like supercapacitors, the redox reactions in the bulk material greatly contributes to the charge storage mechanism.

Metal phosphates are an important class of materials that have been used in chemical conversion[10], hydrogenation of nitro compound[11], electrochemical water splitting[12, 13], and chemical oxidation.[14, 15] In recent years, they have emerged as potential electrode materials for energy storage devices, such as LIBs[16, 17] and supercapacitors.[18, 19] This is because they possess unique layered structures with many channels and cavities, rich redox behaviour arising from the multivalent nature of phosphorus, and good chemical stability arising from the P−O covalent bonding.[19] Controlling the crystal phase, size, and shape of metal phosphates is paramount for optimizing their electrochemical performance for energy storage applications, such as

supercapacitors. Recently, amorphous metal phosphates have attracted increasing interest for supercapacitors because of their short-range structural ordering, high density of active sites (arising from rich defect sites), and good ionic conductivity.[20, 21] Previously, Xi *et al.*[21] reported the synthesis of amorphous $Co_3(PO_4)_2$ nanosheets from the solvothermal reaction of oleylamine-coated $Co(NO_3)_2$ solution with sodium hypophosphate (NaH_2PO_4). These nanosheets exhibited a high specific capacitance of 1174 F g^{-1} at a current density of 2 A g^{-1}. Amorphous cobalt hydrogen phosphate (ACHP) flower-like nanosheets were achieved *via* the hydrothermal reaction of hydrated cobalt chloride solution with polyvinylpyrrolidone (PVP) and sodium hexametaphosphate as the phosphate source.[22] The ACHP nanosheets possessed a specific capacitance of 411.2 F g^{-1} at 1 A g^{-1}. In another report, amorphous vanadyl phosphate ($VOPO_4{\cdot}2H_2O$) nanosheets were obtained from the exfoliation of bulk $VOPO_4{\cdot}2H_2O$ and hybridized with graphene nanosheets.[23] The resulting $VOPO_4{\cdot}2H_2O$/graphene hybrid showed a specific capacitance of 483 F g^{-1} at a current density of 1 A g^{-1}. Despite the progress in this field, the fabrication of amorphous bimetallic phosphates from metal-containing organic precursors is challenging and the size tuning of such materials (*i.e.*, achieving good size monodispersity) is more difficult than the shape control.

In this work, we demonstrate the fabrication of amorphous nickel-cobalt phosphate plate-like particles *via* the solvothermal reaction between nickel-cobalt glycerate spheres in ethanol at 180 °C followed by calcination in air at 600 °C. By changing the solvent from ethanol to ethanol/butanol and ethanol/water mixtures during the solvothermal reaction, the size and morphology of the nickel-cobalt phosphate precursor (labelled as NiCo-TEP) can be controlled. Specifically, the precursor obtained from the solvothermal reaction in ethanol (labelled as E-NiCo-TEP) exhibit plate-like particles with rough edges due to the adsorption of ethyl glycerate (*i.e.*, structure-directing agent) generated from the reaction between the ethyl group from ethanol and glycerate ions.[13] In comparison, the precursors obtained from the solvothermal reaction in ethanol/butanol (named B-NiCo-TEP) and ethanol/water (named W-NiCo-TEP) mixtures exhibit plate-like and rod-like morphology, respectively. When evaluated as potential electrode materials for supercapacitors, the calcined E-NiCo-TEP sample (E-NiCo-TEP-600) shows a higher specific capacity of 620 C g^{-1} (specific capacitance of 1550 F g^{-1}) at 2 A g^{-1} compared to 219 C g^{-1} (548 F g^{-1}) and 85 C g^{-1} (169 F g^{-1}) for B-NiCo-TEP-600 and W-NiCo-TEP-600, respectively. To further demonstrate the practicality, an ASC was fabricated

using commercial AC as the anode and E-NiCo-TEP-600 as the cathode. The E-NiCo-TEP-600//AC ASC exhibits a maximum energy density of 45 Wh kg^{-1} at a power density of 750 W kg^{-1}. Furthermore, this ASC is highly stable with ~100% capacitance retention after 5000 cycles at 10 A g^{-1}. These results highlight the promising potential of these amorphous nickel-cobalt phosphate particles for battery-like supercapacitors.

2. Experimental Procedures

2.1. Chemicals

Nickel nitrate hexahydrate ($Ni(NO_3)_2{\cdot}6H_2O$, 99.9%), cobalt nitrate hexahydrate ($Co(NO_3)_2{\cdot}6H_2O$, 99.9%), triethyl phosphate (TEP; $C_6H_{15}O_4P$, ≥99.8%) and Nafion solution (~5 wt.% in lower aliphatic alcohols and water, contained 15-20% water) were purchased from Sigma Aldrich (Singapore). Ethanol (C_2H_6O, 99.5%), 2-propanol (C_3H_8O, 99.5%), 1-butanol (99.8%), and glycerol ($C_3H_8O_3$, ≥99.5%) were purchased from Merck (Singapore). All reagents were used as received without any further purification.

2.2. Preparation of nickel-cobalt glycerate spheres

The spherical nickel-cobalt glycerate spheres were synthesized according to our previous works.[12, 24, 25] In a typical process, the mixed metal precursor solution was initially prepared by dissolving 0.5 mmol of $Ni(NO_3)_2{\cdot}6H_2O$ and 0.5 mmol of $Co(NO_3)_2{\cdot}6H_2O$ in 40 mL of 2-propanol. Following dissolution, 8 mL of glycerol was added into the mixed metal precursor solution and stirred until a clear pink solution was achieved. This mixture solution was placed into a 100 mL Teflon-lined stainless-steel autoclave and heated at 180 °C for 16 h. After cooling down, the precipitate was collected and washed several times with ethanol to remove unwanted residues. Finally, the nickel-cobalt glycerate spheres were obtained after drying at 60 °C overnight.

2.3 Conversion of nickel-cobalt glycerate spheres to nickel-cobalt phosphate

The conversion of the nickel-cobalt glycerate spheres to nickel-cobalt phosphate precursor (NiCo-TEP**)** was achieved using a simple solvothermal method. In a typical process, 30 mg of the nickel-cobalt glycerate spheres was dispersed in 20 mL of ethanol by ultrasonication. Next, 0.8 mL of TEP was added to the suspension and slowly stirred for 2 h. The suspension was then transferred to a 100 mL stainless-steel autoclave and heated at 180 °C for 8 h. After naturally cooled to room temperature, the product was collected and rinsed with ethanol several times. The washed product was then dried at 60 °C overnight and labelled as

E-NiCo-TEP (E = ethanol). To study the effects of solvent on the size and morphology, two additional nickel-cobalt phosphate precursors were prepared by replacing 5 mL of ethanol with 5 mL of butanol and 5 mL of water, and these precursors were labelled as B-NiCo-TEP and W-NiCo-TEP (B = butanol and W= water), respectively. To obtain nickel-cobalt phosphate, the three precursors (E-NiCo-TEP, B-NiCo-TEP, and W-NiCo-TEP) were calcined in air at 600 °C for 2 h with a slow heating rate of 1 °C min^{-1}. The calcined products were named E-NiCo-TEP-600, B-NiCo-TEP-600, and W-NiCo-TEP-600.

2.4 Characterization

The phase compositions of the samples were analyzed using the Bruker D8 Advanced X-ray diffractometer (XRD) with Cu-Kα radiation (λ = 1.54 Å). The morphology of the samples was observed using both field emission scanning electron microscope (FESEM, Hitachi SU8000) and transmission electron microscope (TEM, Hitachi7700). Fourier transform infrared (FTIR) spectra of the samples were collected using IR Prestige 21 (Shimadzu, Japan). Nitrogen (N_2) sorption measurements were conducted using a BELSORP-mini II sorption system (BEL, Japan). The measurements were performed at 77 K and all samples were degassed at 120 °C for 12 h prior to the measurements. The specific surface area and pore size distribution of the samples were estimated using Brunauer- Emmett-Teller (BET) and Barret-Joyner-Halenda (BJH) techniques, respectively. The surface elemental analyses of the samples were carried out using Kratos Axis Ultra photoelectron spectrometer with Al Kα X-rays (1486.6 eV). The high-resolution XPS spectra were calibrated with reference to the C 1s peak at 285 eV.

2.5 Electrochemical performance

The electrochemical measurements of the bimetallic phosphate samples were carried out using a standard three-electrode system using a CHI 660E electrochemical workstation. Silver/silver chloride (Ag/AgCl) (in sat. KCl) and platinum wire were used as the reference and counter electrodes, respectively, while carbon cloth and 6.0 M KOH were used as the current collector and electrolyte, respectively. To fabricate the working electrode, 4 mg of the bimetallic metal phosphate sample was dispersed in 950 µL of water/2-propanol mixture solution (3:1 *v*/*v*). Next, 50 µL of Nafion was added to the suspension and sonicated until a uniform suspension of 4.0 mg mL^{-1} was achieved. Following this, 250 µL of the metal phosphate suspension was dropped onto a carbon paper (1 cm x 1 cm) and dried naturally. The electrochemical properties, including the specific

capacitance and its related mechanism, were evaluated by the cyclic voltammetry (CV) technique at a potential window of 0-0.5 V. The specific capacity (Q) in C g^{-1} was calculated from the CV curve using Eq. (1)[26]:

$$Q = \frac{\int IdV}{2mv} \quad (1)$$

where I, m, and v are current (A), mass of the active material (g), scan rate (mV s^{-1}), and potential window, respectively. The specific capacity of the electrode material was also calculated from the galvanostatic charge-discharge (GCD) curve using Eq. (2)[27, 28]:

$$Q = \frac{I\Delta t}{m} \quad (2)$$

In the above equation, Δt represents the discharge time (s). In addition, electrochemical impedance spectroscopy (EIS) was also carried out to evaluate the charge transfer resistance (R_{ct}) of all samples. The EIS measurements were carried out in the frequency range of 1 kHz-0.01 Hz, amplitude of 0.005 V, and applied voltage of 0.3 V.

An asymmetric supercapacitor (ASC) was also assembled by employing commercial activated carbon (AC) as the negative electrode and E-NiCo-TEP-600 as the positive electrode with the weight ratio AC:E-NiCo-TEP-600 = 4:1 and 6 M KOH as the electrolyte. The mass loading of the positive and negative electrodes was calculated using Eq. (3):

$$\frac{m_1}{m_2} = \frac{Q_2 \Delta V_2}{Q_1 \Delta V_1} \quad (3)$$

The energy density (E) and power density (P) of the ASC were calculated using Eqs. (4) and (5):

$$E = \frac{0.5 C \Delta V^2}{3.6} \quad (4)$$

$$P = \frac{E\ x\ 3600}{\Delta t} \quad (5)$$

where C is the specific capacitance of the ASC (F g^{-1}), E is the energy density (Wh kg^{-1}), and P is the power density (W kg^{-1}).

3. Results and discussion

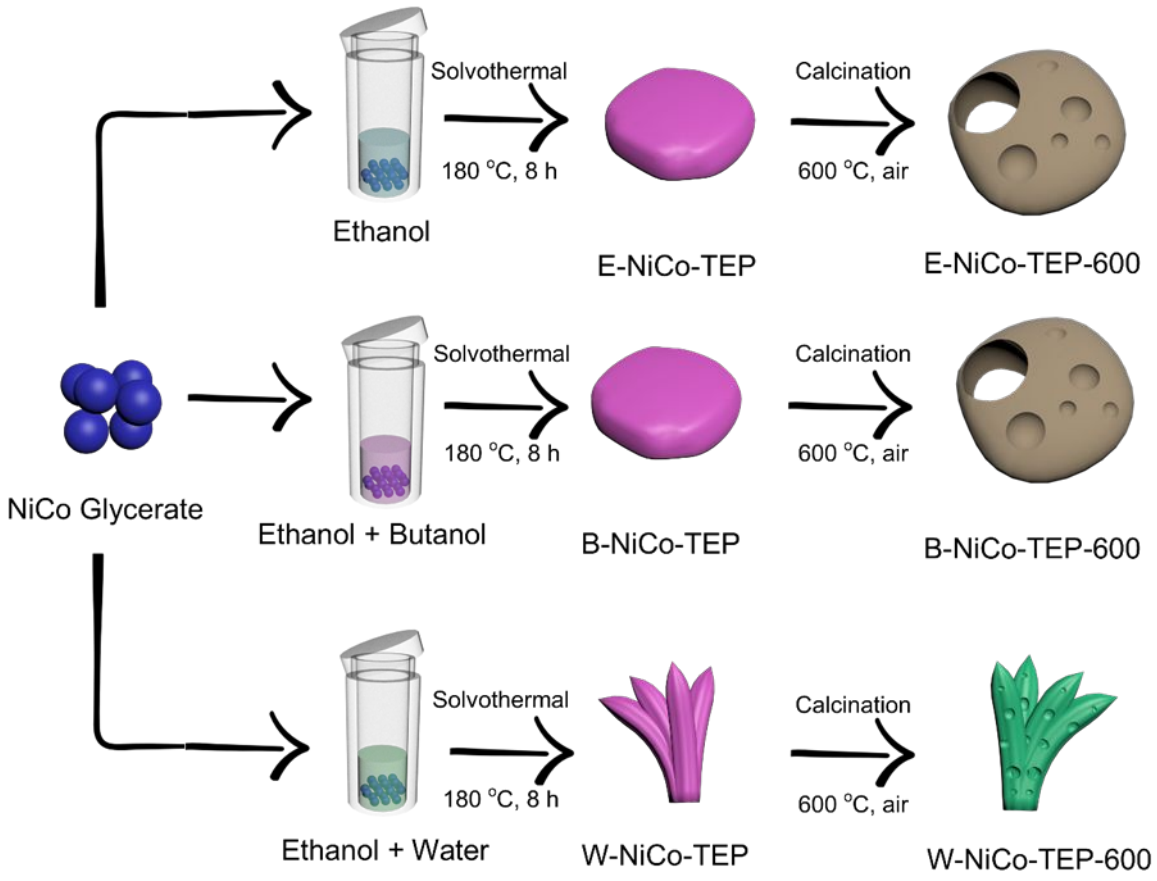

Scheme 1. Schematic illustration showing the fabrication steps of the three nickel-cobalt phosphate samples (E-NiCo-TEP-600, B-NiCo-TEP-600, and W-NiCo-TEP-600) from nickel-cobalt glycerate spheres.

The fabrication process of the three nickel-cobalt phosphate samples (E-NiCo-TEP-600, B-NiCo-TEP-600, and W-NiCo-TEP-600) from nickel-cobalt glycerate spheres is illustrated in **Scheme 1**. In this work, monodisperse nickel-cobalt phosphate precursors (NiCo-TEP) with various morphology are synthesized *via* the solvothermal reactions of nickel-cobalt glycerate spheres with TEP (as the phosphate precursor) in different solvents at 180 °C for 8 h. As seen in **Fig. S1**, the nickel-cobalt glycerate sample displays a uniform spherical morphology with diameters in the narrow range of 400-500 nm. The nickel-cobalt glycerate sample exhibits a broad peak at around 12° which is the typical characteristic of metal glycerates (**Fig. S2a**).[12, 24] The nickel-cobalt phosphate precursor (E-NiCo-TEP) obtained from the solvothermal reaction of nickel-cobalt glycerate spheres with TEP in pure ethanol is mostly amorphous with only a single sharp peak observed at 7.3° (**Fig. 1a (i)**). In comparison, the B-NiCo-TEP sample achieved using the ethanol/butanol mixture is

weakly crystalline. The XRD patterns of E-NiCo-TEP and B-NiCo-TEP (**Fig. 1a (i, ii)**) show sharp peaks at 7.3°and 6.5°, respectively. Due to the lack of peaks, the exact crystal structure is difficult to determine for these samples. However, the strong peak at 7.3° in E-NiCo-TEP and the major peaks at 6.5° and 12.5° in B-NiCo-TEP resemble the XRD peaks of metal phosphate materials reported in previous studies which displayed an orthorhombic crystal structure (JCPDS No. 00-049-2391).[29, 30] Based on the assumed crystal structure, the interlayer spacings of E-NiCo-TEP and B-NiCo-TEP are measured at ~12.0 nm and 13.4 nm, respectively.[13] Among them, W-NiCo-TEP has the lowest crystallinity, indicating that water can disturb the layered structure of the crystal.

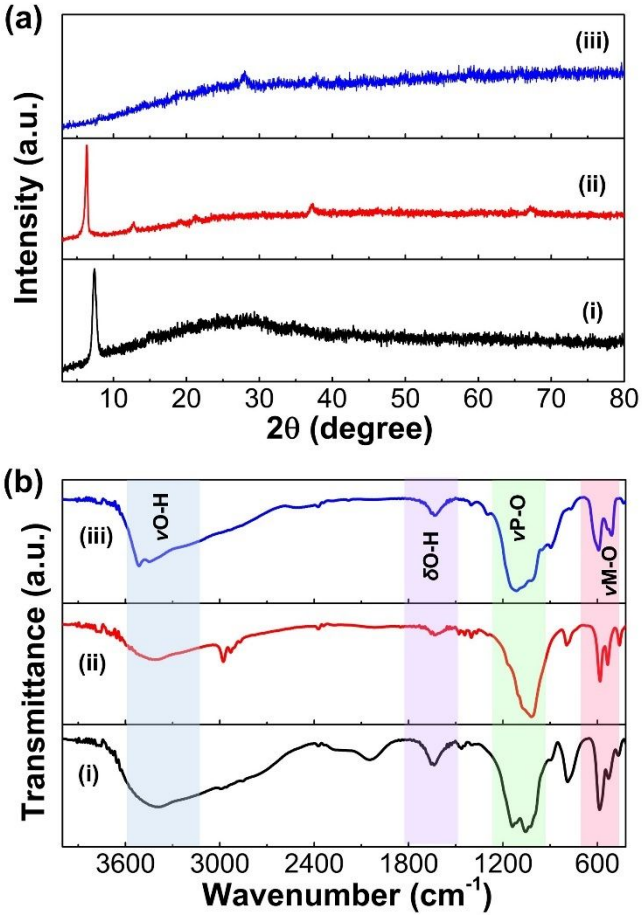

Fig. 1. (a) XRD patterns and (b) FTIR spectra of (i) E-NiCo-TEP, (ii) B-NiCo-TEP, and (iii) W-NiCo-TEP.

Furthermore, we have employed other characterization techniques, such as FTIR spectroscopy to identify the chemical bonding present in these samples. For nickel-cobalt glycerate spheres, the broad IR band at around 3400 cm^{-1} corresponds to the O−H stretching vibration (**Fig. S2b**). The IR bands in the range of 2850-2950 cm^{-1} are attributed to the stretching vibration of C−H group.[31] The C=O and C=C stretching

vibrations are marked by the presence of IR bands at 1644 cm^{-1} and 1590 cm^{-1}, respectively. Moreover, the IR bands at 1403 cm^{-1} and 1044 cm^{-1} are indexed to C−H bending and C−O stretching vibrations, respectively. Meanwhile, the IR bands at 1115 cm^{-1} and 937 cm^{-1} correspond to $-CH_2$ bending and C−C stretching vibrations, respectively, while the IR bands in the range 436-583 cm^{-1} can be assigned to Ni/Co−O stretching vibration.

As depicted in **Fig. 1b**, the FTIR spectra of E-NiCo-TEP, B-NiCo-TEP, and W-NiCo-TEP have some similarities as well as differences which may be due to the use of different solvents. The three samples share a similar broad IR band at ~3400 cm^{-1} associated with the O−H stretching vibration from adsorbed water molecules. The additional band at ~3500 cm^{-1} in W-NiCo-TEP, is attributed to the O−H vibration from the coordination between Ni and Co metals and water during the solvothermal reaction.[32-34] The symmetric stretching vibration of C−H from the ethyl group is clearly observed at 2974 cm^{-1}, especially in B-NiCo-TEP.[35] This band is very weak in E-NiCo-TEP and not observed in W-NiCo-TEP. The IR band at 1135 cm^{-1} in E-NiCo-TEP is associated with the P−O stretching vibration. This band is slightly shifted to 1119 cm^{-1} in the W-NiCo-TEP sample. Moreover, the C−O−P stretching vibrations are observed at 1045 cm^{-1} and 1022 cm^{-1} for E-NiCo-TEP, 1066 cm^{-1} and 1019 cm^{-1} for B-NiCo-TEP, and 1016 cm^{-1} and 1071 cm^{-1} for W-NiCo-TEP.[36, 37] The strong IR band at around 781 cm^{-1} in E-NiCo-TEP is attributed to the P−C stretching vibration. This band is weaker in B-NiCo-TEP and W-NiCo-TEP.[38] The interaction between Ni and Co metals and TEP is indicated by the IR bands located in the range of 400-500 cm^{-1}. The metal binds to TEP through the oxygen group as the P=O stretching vibration in pure TEP at 1297 cm^{-1} is not detected in all samples, indicating that the P=O bond may be changed to P−O, as seen from the FTIR spectra comparison of E-NiCo-TEP and pure TEP (**Fig. S3**).

Fig. 2 shows the SEM images of the resulting NiCo-TEP samples obtained from the solvothermal reaction of nickel-cobalt glycerate spheres with TEP in different solvents. The E-NiCo-TEP sample (**Fig. 2a-c)** shows a highly uniform plate-like morphology with rough edges. These nanoplates are highly monodisperse in size with a narrow diameter distribution in the range of 300-380 nm, as seen in **Fig. 2d**. Similarly, the B-NiCo-TEP sample (**Fig. 2e-g**) also consists of nanoplates, however they are not as well-separated as E-NiCo-TEP and are stacked vertically. These nanoplates possess smoother edges and smaller diameters (~140-190

nm) compared to E-NiCo-TEP (**Fig. 2h)**. These observations suggest that the addition of butanol helps to slow down the lateral growth of these nanoplates. In contrast, W-NiCo-TEP has a rod-like morphology, as shown in **Fig. 2i-k.** These results indicate that the addition of water promotes the morphological transformation from a plate-like structure to a rod-like structure, as seen in **Fig. 2l**.

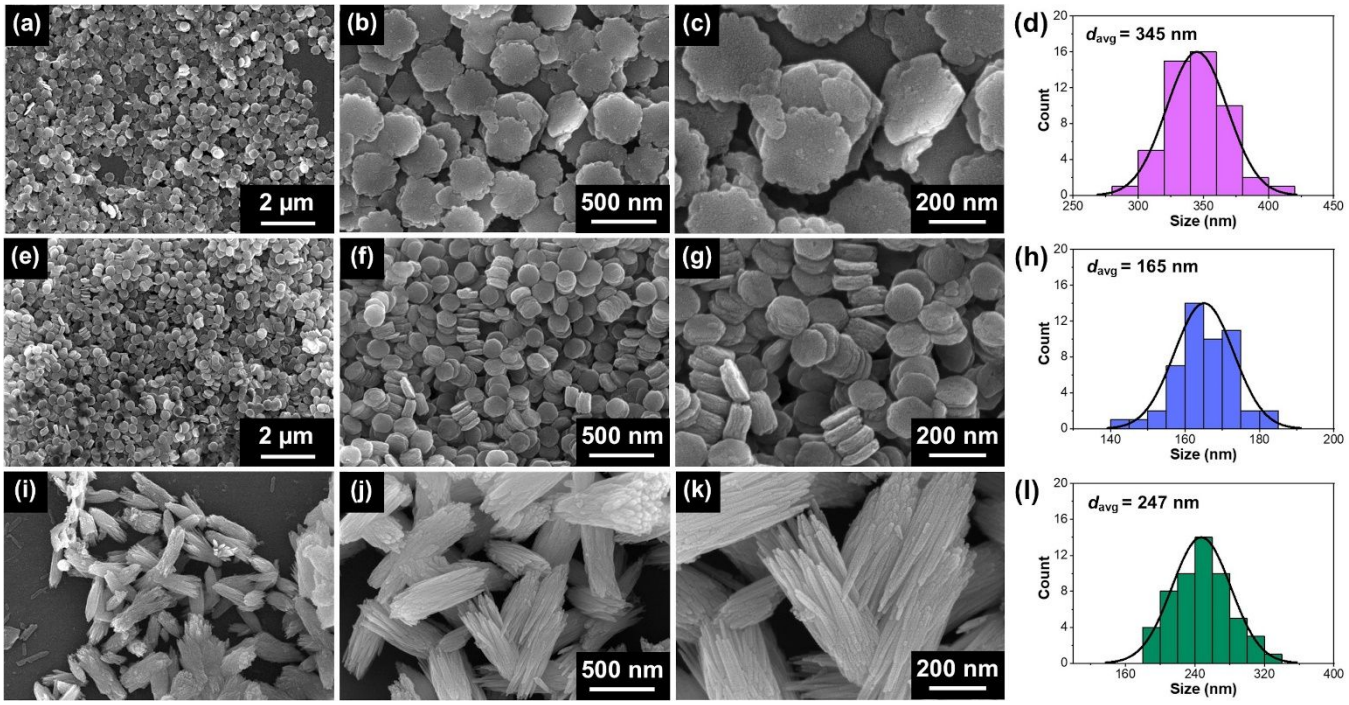

Fig. 2. Low- and high-magnification SEM images and size distribution histograms for (a-d) E-NiCo-TEP, (e-h) B-NiCo-TEP, and (i-l) W-NiCo-TEP, respectively.

The possible formation mechanism of the 2D NiCo-TEP nanoplates can be explained as follows. During the solvothermal reaction with TEP, the nickel-cobalt glycerate spheres initially dissociate into Ni^{2+} and Co^{2+} ions and glycerate ions. In the presence of ethanol, glycerate ions are likely to react with the ethyl group from ethanol to form ethyl glycerate by releasing OH^- ions.[13] This hydroxyl group induces the formation of diethyl phosphate (DEP) by releasing one of their ethoxy intermediate groups and attaching OH^-.[39] At the final stage, the DEP can interact with Ni^{2+} and Co^{2+} ions to form NiCo-DEP and releases water as a product.[40] In this case, the ethoxy intermediate is considered to be stable in ethanol.[41] In the case of E-NiCo-TEP and B-NiCo-TEP nanoplates, ethyl glycerate may adsorb on the surface and limit the growth in the vertical direction, leading to the formation of monodisperse plate-like particles. In comparison, for W-NiCo-TEP, ethyl glycerate is not formed and a similar mechanism is also proposed here when ethanol is partially replaced by butanol.

However, since butanol is less reactive and has a higher boiling point than ethanol, more energy is required to induce the formation of butyl glycerate and the energy from the solvothermal reaction at 180 °C may not be sufficient to promote its formation.[42, 43] As a result, the availability of OH^- ions is reduced leading to the reduction in the yield and average diameter of the nanoplates in B-NiCo-TEP-600. Different results are obtained when water is used to partially replace ethanol in the reaction.

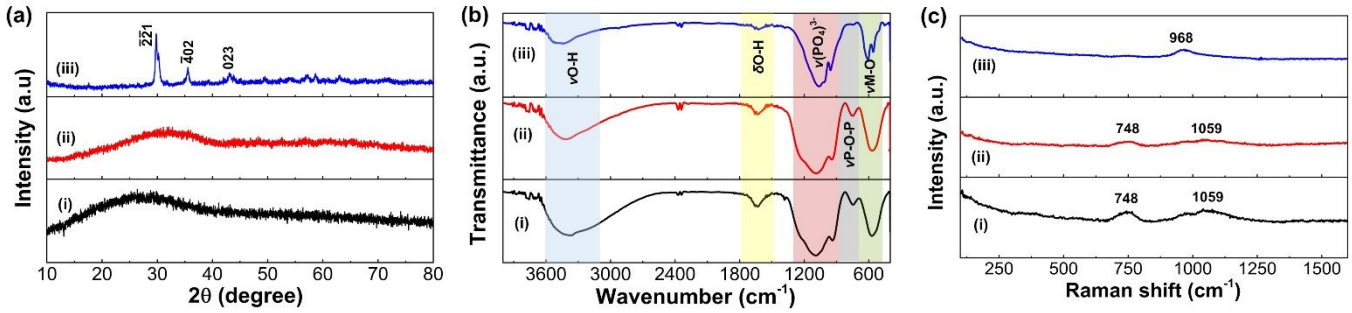

Fig. 3. (a) XRD patterns, (b) FTIR spectra, and (c) Raman spectra of (i) E-NiCo-TEP-600, (ii) B-NiCo-TEP-600, and (iii) W-NiCo-TEP-600.

Unlike E-NiCo-TEP and B-NiCo-TEP, the IR band at 3570 cm^{-1} only appears in W-NiCo-TEP (**Fig. 1b**). This band can be assigned to the stretching vibration of O−H group from metal hydroxide. The presence of this band suggests that a mixture of nickel-cobalt hydroxide and NiCo-DEP is present in this sample. Moreover, a water-TEP complex may also have been formed as the band at 887 cm^{-1} appears in W-NiCo-TEP, which may be indexed to the P−O−C stretching vibration originating from the water-TEP complex.[44] In the case of W-NiCo-TEP, apart from ethyl glycerate, glyceric acid may also be formed as a byproduct.[24] Since the formation of DEP is induced by the presence of OH^- ions from the reaction between the ethyl group and glycerate ions, replacing ethanol fully with water cannot produce any product as all the glycerate ions may be converted to glyceric acid and OH^- ions are more likely to coordinate with the positively charged metal (Ni^{2+} and Co^{2+}) ions. Therefore, NiCo-DEP is not obtained, and the nickel-cobalt hydroxide precipitate may be dissolved due to the highly acidic environment (the pH of the supernatant obtained from the solvothermal reaction in water/ethanol mixture is 2.04). To prove this hypothesis, we dissolved a nickel-cobalt hydroxide powder in this acidic supernatant and found that it dissolves rapidly (**Fig. S4**), thus confirming our hypothesis.

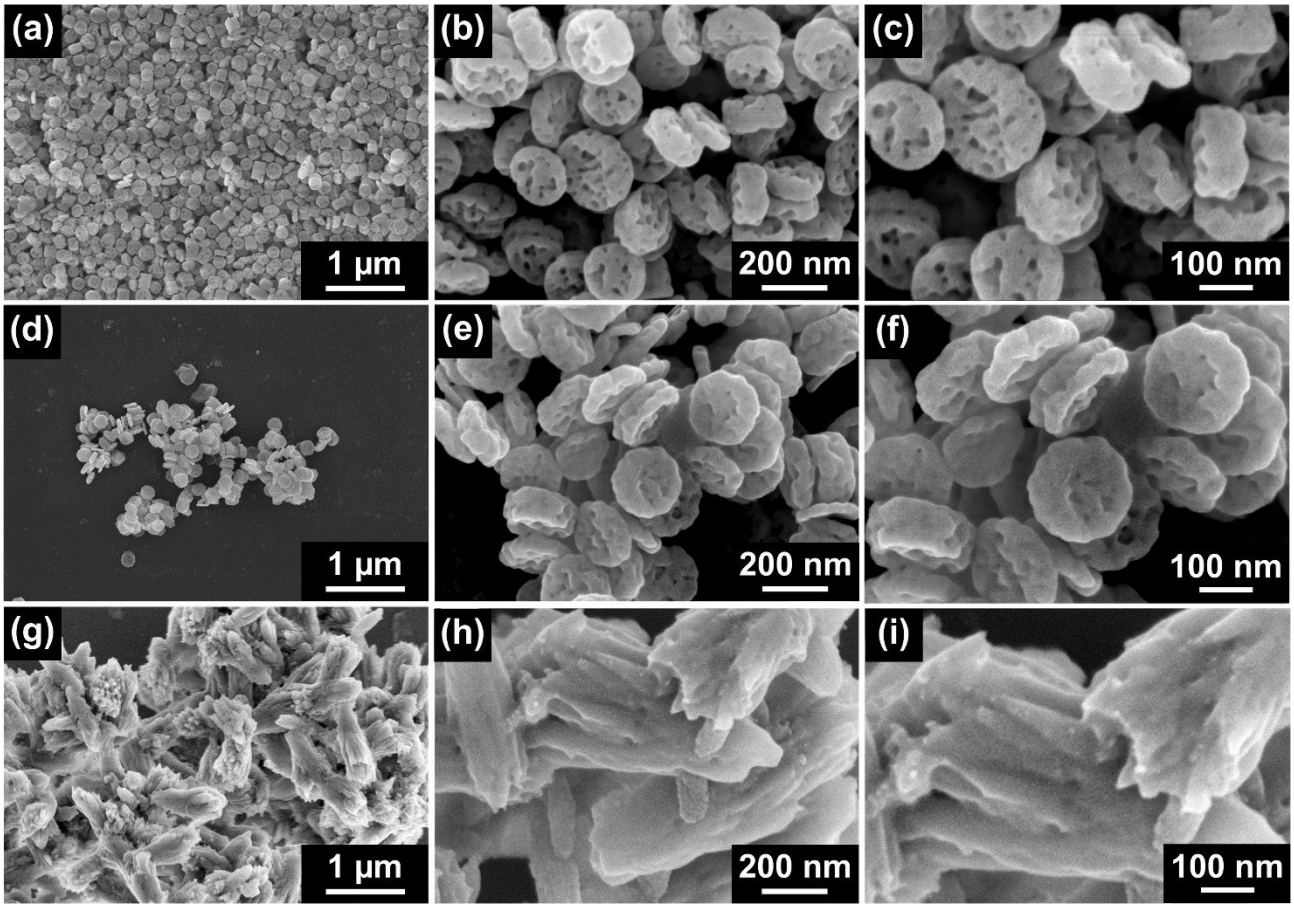

Fig. 4. SEM images of (a-c) E-NiCo-TEP-600 and (d-f) B-NiCo-TEP-600, and (g-i) W-NiCo-TEP-600 obtained from the calcination of E-NiCo-TEP, B-NiCo-TEP, and W-NiCo-TEP in air at 600 °C, respectively.

The NiCo-TEP precursors can be transformed into nickel-cobalt phosphate by calcining them in air at 600 °C. **Fig. 3a** displays the XRD patterns of the samples obtained after calcination. The E-NiCo-TEP-600 and B-NiCo-TEP-600 samples are largely amorphous (**Fig. 3a (i, ii)**). The TG-DTA measurements of E-NiCo-TEP and B-NiCo-TEP reveal the presence of an endothermic peak with a significant weight loss at ~400 °C due to the removal of organic constituents from these samples and the conversion to nickel-cobalt phosphate (**Fig. S5a, b**). The conversion of the nickel-cobalt phosphate phase to nickel-cobalt pyrophosphate is indicated by an exothermic peak at 700 °C. For W-NiCo-TEP-600, several peaks belong to $NiCo(PO_4)_3$ (ICSD No. 37136) are observed, indicating that crystalline $NiCo(PO_4)_3$ can be obtained by involving water in the synthesis process (**Fig. 3a (iii)**).[45] Interestingly, the TG-DTA curve of W-NiCo-TEP (**Fig. S5c**) shows a different thermal decomposition behavior with no strong endothermic peak and weight loss occurring gradually.

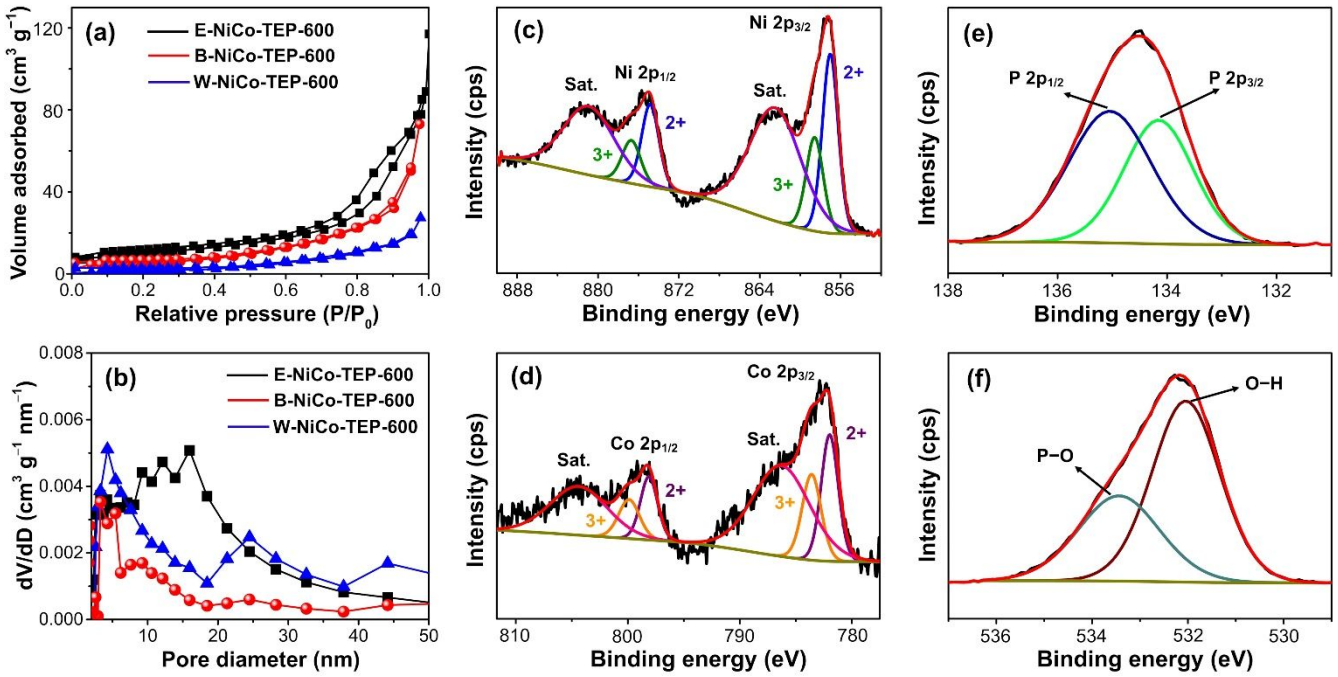

Fig. 5. (a) N_2 adsorption-desorption isotherms of E-NiCo-TEP-600, B-NiCo-TEP-600, and W-NiCo-TEP-600 and (b) the corresponding pore size distribution plots. High resolution XPS spectra for (c) Ni 2p, (d) Co 2p, (e) P 2p, and (f) O 1s of E-NiCo-TEP-600.

To confirm the presence of nickel-cobalt phosphate in the calcined samples, FTIR measurements were carried out and the results are shown in **Fig. 3b**. All three samples (E-NiCo-TEP-600, B-NiCo-TEP-600, and W-NiCo-TEP-600) show the broad band belonging to O–H stretching vibration at ~3200-3600 cm^{-1}.[19, 46] The IR band at 1625 cm^{-1} in the FTIR spectrum of E-NiCo-TEP-600 is attributed to the O–H bending vibration.[39] The intensity of this band is decreased in B-NiCo-TEP-600 and W-NiCo-TEP-600. Further, in all three calcined samples, the IR bands in the ranges of ~1060-1095 cm^{-1} and ~930-960 cm^{-1} correspond to anti-symmetric and symmetric stretching vibrations of PO_4^{3-}, respectively. In addition, the IR bands at ~748 cm^{-1}, 564 cm^{-1}, and 553 cm^{-1} can be assigned to P–O–P stretching, O–P–O bending, and PO_4^{3-} out-of-plane bending vibration, respectively.[13, 39] In addition, the Raman spectra in **Fig. 3c** also confirm the formation of metal phosphates in all three samples. The relatively weak Raman bands at around 748 cm^{-1} and 1059 cm^{-1} in E-NiCo-TEP-600 and B-NiCo-TEP-600 (**Fig. 3c (i, ii)**) can be assigned to the symmetric vibration of P–O–P and the v_3 stretching mode of $(PO_4)^{3-}$, respectively.[47, 48] In W-NiCo-TEP-600, only a single Raman band is observed at 968 cm^{-1} which is attributed to the v_1 stretching mode $(PO_4)^{3-}$ (**Fig. 3c (iii)**). This may be

linked to the disturbance of the layered crystal structure by water (**Fig. 1a (iii))** The presence of IR bands corresponding to the phosphate group in both FTIR and Raman spectra of these three samples imply that they are composed of nickel-cobalt phosphate.

Fig. 4 displays the morphology of the NiCo-TEP samples after calcination in air at 600 °C. Both E-NiCo-TEP-600 (**Fig. 4a-c)** and B-NiCo-TEP-600 (**Fig. 4d-f**) show porous plate-like morphology with a relatively comparable particle size. In comparison, the rod-like particles (W-NiCo-TEP-600) aggregate with each other following the calcination process (**Fig. 4g-i**). In agreement with the SEM observations, the TEM and STEM images of E-NiCo-TEP-600 also show the porous plate-like morphology which originated from the removal of ethyl group during calcination (**Fig. S6a**, **b)**. The EDS mapping of E-NiCo-TEP-600 reveals the uniform distribution of Ni, Co, O, and P elements in this sample, as seen in **Fig. S6c-f**. The porous nature of all three calcined samples is supported by the N_2 adsorption-desorption isotherms shown in **Fig. 5**. The specific surface area and pore volume of E-NiCo-TEP-600 are 35 $m^2\ g^{-1}$ and 0.13 $cm^3\ g^{-1}$, respectively, which are higher than those of B-NiCo-TEP-600 (19 $m^2\ g^{-1}$ and 0.11 $cm^3\ g^{-1}$) and W-NiCo-TEP-600 (3.5 $m^2\ g^{-1}$ and 0.04 $cm^3\ g^{-1}$) (**Fig. 5a**). Moreover, the pore size distribution data of these three samples indicate that they contain mostly mesopores (**Fig. 5b)**.

The surface chemical compositions and electronic states of the optimum sample, E-NiCo-TEP-600, were analyzed by XPS. The XPS survey spectrum of E-NiCo-TEP-600 confirms the presence of Ni, Co, P, and O elements, as seen in **Fig. S7**. The carbon element in this spectrum originates from substrate contamination during the XPS measurement as no carbon is detected from the EDS mapping of E-NiCo-TEP-600 (**Fig. S6**). The deconvoluted Ni 2p spectrum of E-NiCo-TEP-600 shows the Ni^{2+} peaks at 857.0 eV and 874.8 eV and the Ni^{3+} peaks at 858.6 eV and 876.7 eV with the corresponding satellite peaks at 862.5 eV and 880.9 eV, respectively, as seen in **Fig. 5c**. The peaks at 853.33 eV and 871.16 eV signal the presence of Ni^{2+}.[45, 49] The deconvolution of the Co 2p spectrum of E-NiCo-TEP-600 in **Fig. 5d** shows the existence of Co^{2+} peaks at 782.0 eV and 798.1 eV as well as Co^{3+} peaks at 783.6 eV and 799.9 eV with satellite peaks at 786.3 and 804.4 eV.[50, 51] Moreover, the deconvoluted P 2p spectrum of E-NiCo-TEP-600 features two peaks at 134.15 eV and 135.04 eV corresponding to P $2p_{3/2}$ and P $2p_{1/2}$, respectively, which are indicative of P(V) (**Fig. 5e**). For O 1s spectrum, the deconvolution reveals two peaks at 532.0 eV and 533.4 eV attributed to structural water (O−H)

and core level of oxygen in phosphate species (P−O), respectively (**Fig. 5f**).[52] These XPS results further solidify that E-NiCo-TEP-600 is essentially nickel-cobalt phosphate.

3.2. Electrochemical Performance

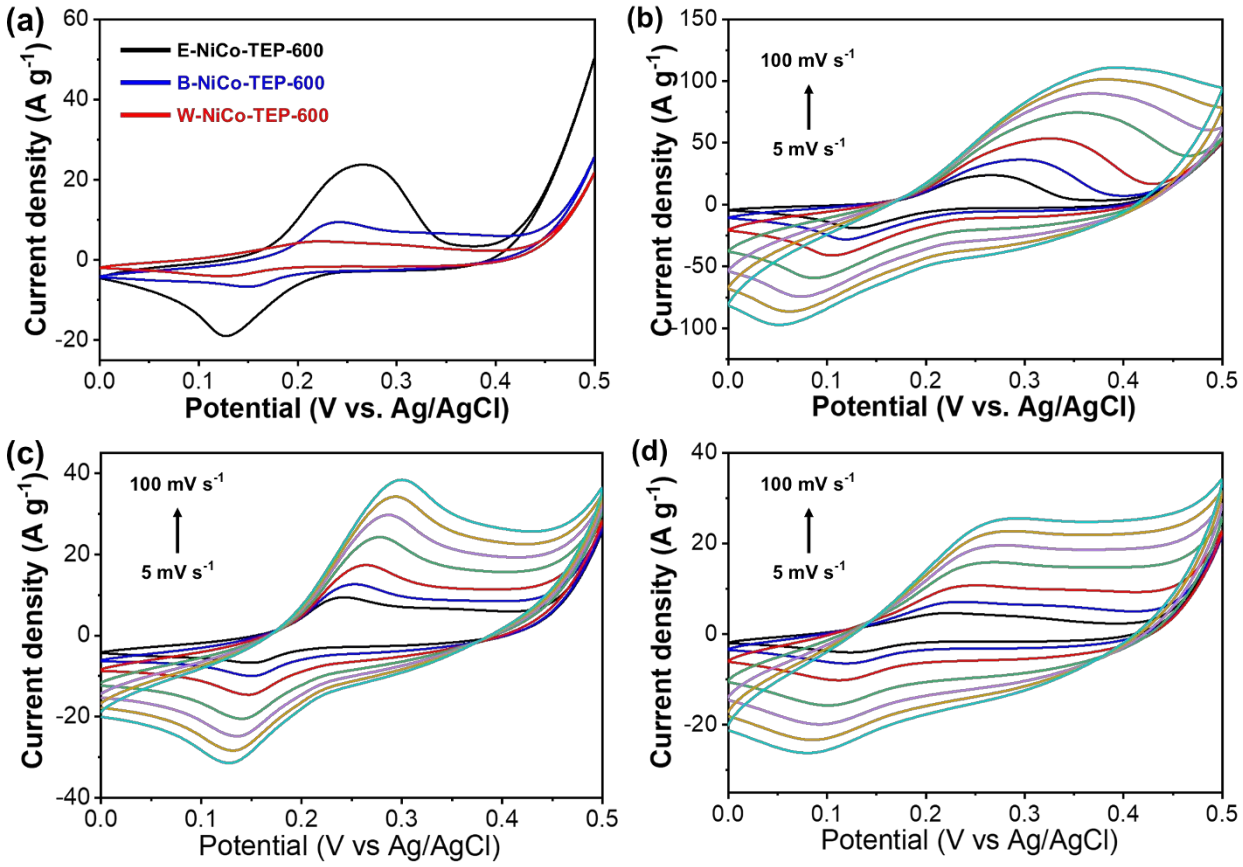

Fig. 6. (a) CV profiles of E-NiCo-TEP-600, B-NiCo-TEP-600, and W-NiCo-TEP-600. The effect of scan rate on the CV profile of (b) E-NiCo-TEP-600, (c) B-NiCo-TEP-600, and (d) W-NiCo-TEP-600. The CV measurements were carried out in 6.0 M KOH in the potential range of 0-0.5 V vs. Ag/AgCl.

The electrochemical performance of the calcined bimetallic phosphate samples (E-NiCo-TEP-600, B-NiCo-TEP-600, and W-NiCo-TEP-600) was evaluated firstly by the CV technique using a three-electrode system in a 6.0 M KOH electrolyte. The CV curves were recorded in the potential range of 0-0.5 V vs. Ag/AgCl, and the scan rate was varied from 5 to 100 mV s^{-1}. **Fig. 6** shows the CV profiles of E-NiCo-TEP-600, B-NiCo-TEP-600, and W-NiCo-TEP-600 at a scan rate of 5 mV s^{-1}. The CV curves of these samples show a couple of peaks originating from oxidation and reduction reactions on their surfaces. The presence of the Faradaic region suggest that all the samples exhibit battery-like behaviour. The morphology of the bimetallic nickel-

cobalt phosphate samples affects the electrochemical performance. The current of E-NiCo-TEP-600 is higher than that of other samples, especially W-NiCo-TEP-600. Based on the CV measurements, the specific capacities are calculated to be 582 C g^{-1}, 298 C g^{-1}, and 188 C g^{-1} for E-NiCo-TEP-600, B-NiCo-TEP-600, and W-NiCo-TEP-600, respectively, with their corresponding specific capacitances being 1163 F g^{-1}, 595 F g^{-1}, and 377 F g^{-1} at a scan rate of 5 mV s^{-1}.

The electrochemical performance of these three phosphate samples was also evaluated by GCD measurements at various current densities from 2 to 10 A g^{-1} in the potential range of 0-0.4 V vs. Ag/AgCl. Based on the GCD measurements, the specific capacities of E-NiCo-TEP-600, B-NiCo-TEP-600, and W-NiCo-TEP-600 at a current density of 2 A g^{-1} are 620, 219, and 84.5 C g^{-1}, respectively, equivalent to specific capacitances of 1550, 548, and 169 F g^{-1} (**Fig. 7a**), indicating the superior electrochemical performance of E-NiCo-TEP-600. From **Fig. 7b-d**, it can be observed the discharge time, that is proportional to the discharge capacity, of these electrodes decreases with the increase of current density, reflecting the decrease in specific capacity as the current density increases from 2 to 10 A g^{-1}. This is because of a concentration overpotential, that is at high current densities, active sites in the deeper part of the electrode material cannot react effectively due to shortage of OH^- ions. As seen in **Fig. 7e**, E-NiCo-TEP-600 displays specific capacities of 620, 570, 534, 504, and 480 C g^{-1} at current densities of 2, 4, 6, 8, and 10 A g^{-1}, respectively. In comparison, the specific capacities of B-NiCo-TEP-600 are 219, 168, 139, 117, and 101 C g^{-1} at current densities of 2, 4, 6, 8, and 10 A g^{-1}, respectively. Moreover, the specific capacities of W-NiCo-TEP-600 are 85, 57, 43, 34, and 26 C g^{-1} at current densities of 2, 4, 6, 8, and 10 A g^{-1}, respectively. These results reveal the superior electrochemical performance of E-NiCo-TEP-600 compared to the other two samples. This is further supported by the EIS measurements shown in **Fig. S8**. The diameter of the semi-circle observed in the high frequency region represents the charge transfer resistance while the tail at a higher frequency represents the Warburg impedance. Based on the EIS analysis, the smallest charge transfer resistance is achieved by E-NiCo-TEP-600, indicating the faster charge transfer kinetics in this sample. In addition, the Warburg resistance is also a key parameter in determining supercapacitor performance since it is strongly related to the mass transfer or ion diffusion resistance.[53, 54] The Warburg resistance values for E-NiCo-TEP-600, B-NiCo-TEP-600, and W-NiCo-TEP-600, are 219.6 Ω, 228.1 Ω, and 427.6 Ω, respectively, revealing the smaller diffusion resistance in E-NiCo-

TEP-600. Additionally, the E-NiCo-TEP-600 electrode displays good long-term stability with a high capacitance retention of 98.5% after 5000 cycles at a high current density of 10 A g^{-1} (**Fig. 7f).** From T**able 1**, it can be seen that the as-prepared E-NiCo-TEP-600 electrode exhibits better electrochemical performance than many previously reported metal phosphate materials, as seen in **Table 1**.[19, 49, 55-61]

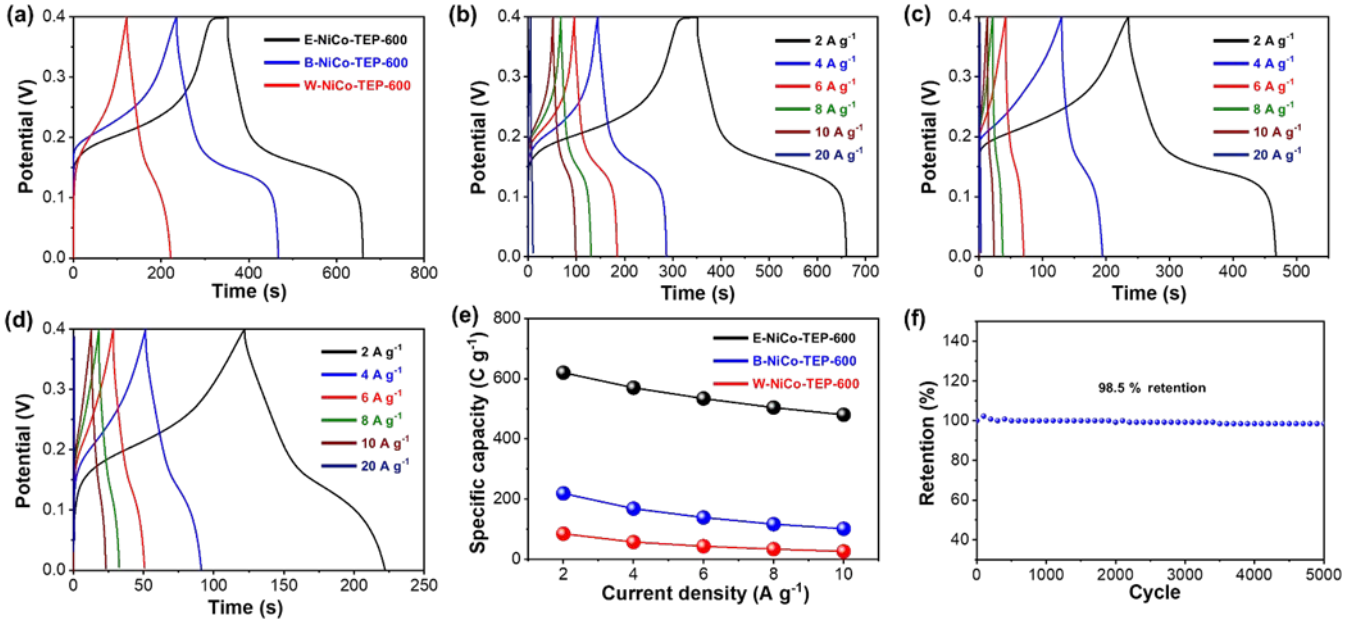

Fig. 7. (a) GCD curves of (a) E-NiCo-TEP-600, B-NiCo-TEP-600, and W-NiCo-TEP-600 at a current density of 2 A g^{-1}. GCD curves of (b) E-NiCo-TEP-600, (c) B-NiCo-TEP-600, and (d) W-NiCo-TEP-600 at current densities of 2, 4, 6, 8, and 10 A g^{-1}. (e) The specific capacity versus current density plots for E-NiCo-TEP-600, B-NiCo-TEP-600, and W-NiCo-TEP-600. (f) Stability test of E-NiCo-TEP-600 for 5000 cycles at a high current density of 10 A g^{-1} by the GCD method.

The good electrochemical performance of E-NiCo-TEP-600 is attributed to several reasons. Firstly, the small size (100-200 nm) of E-NiCo-TEP-600 can reduce the ion diffusion distance and its larger surface area and pore volume compared to B-NiCo-TEP-600 and W-NiCo-TEP-600 may provide better or easier diffusion for OH^- ions (**Fig. S8**). Furthermore, the high structural disorder in this amorphous phosphate material may provide active diffusion channels and allows for easier penetration of electrolyte (OH^-) ions, resulting in a deeper diffusion through the material.[62] Moreover, the long-range disorder of amorphous metal phosphates can provide additional redox sites *via* defects and promote enhanced interactions with OH^- ions.[63]

Additionally, the rich mesopores in E-NiCo-TEP-600 can further improve the diffusion of these ions and promote faster kinetic reactions at the electrolyte/electrode interface, as supported by the EIS data (**Fig. S8**).

In general, the storage mechanism occurred in E-NiCo-TEP-600 is described in Eq. (6):

$$(Ni, Co)_3(PO_4)_2 + OH^- \rightarrow (Ni, Co)_3(PO_4)_2OH + e^- \quad (6)$$

According to the XPS analysis, the surface of E-NiCo-TEP-600 contains a significant amount of hydroxyl groups, which may enhance the interaction between its surface and the aqueous electrolyte. During the storage process, OH^- ions can react with nickel-cobalt phosphate (E-NiCo-TEP-600) on the surface, resulting in the formation of $(Ni, Co)_3(PO_4)_2OH$ and the release of electron for a redox reaction.[49, 64] The existence of $(Ni, Co)_3(PO_4)_2OH$ is confirmed by the FTIR analysis of E-NiCo-TEP-600 after 5000 cycles, as shown in **Fig. S9a**. The intensities of IR bands belonging to phosphate and O−H groups from water decrease. In addition, a new small weak band appears at around 1370 cm^{-1} which may originate from nickel-cobalt phosphate hydroxide.[65, 66] This is further consolidated by the SEM images in **Fig. S9b, c**, in which the plate-like particles of E-NiCo-TEP-600 are covered by nanosheets, which is believed to be $(Ni, Co)_3(PO_4)_2OH$ species originating from the reaction between nickel-cobalt phosphate ($(Ni, Co)_3(PO_4)_2$) with OH^- ions on the surface of this material.

In addition, XPS analysis was also performed to investigate the surface composition of the E-NiCo-TEP-600 electrode after cycling (**Fig. S12**). Based on the XPS spectra, after 5000 cycles, there is no P 2p peak detected on the surface of electrode. This is further supported by the increase in O−H peak intensity and the much lower the P−O peak intensity in O 1s spectrum of E-NiCo-TEP-600 after cycling, indicating that the electrode's surface is covered by the hydroxyl group (further supported by the formation of the typical sheet-like structure of hydroxides in **Fig. S9b, c**).[67] After cycling, the Ni^{2+} peaks are found at lower binding energies of 856.2 eV and 873.5 eV, while the Ni^{3+} peaks are located at 858.0 eV and 875.02 eV. Furthermore, Ni^0 peaks are also observed at binding energies of 852.6 eV and 871.0 eV. In the case of Co, only the Co^{2+} peaks are observed at 780.2 eV and 795.3 eV with two satellites at 782.4 eV and 797.4 eV. The binding energies of the Ni 2p and Co 2p peaks are lowered compared to those before cycling. These results confirm the formation of metal hydroxide species on the surface of this electrode after cycling.[68]

The study on kinetic analysis was conducted by varying the scan rate and calculating the *b* value using Eq. (7)[69]:

$$i_p = av^b \quad (7)$$

where i_p and v are peak oxidation current (A) and scan rate (mV s^{-1}), respectively, while *a* and *b,* are adjustable parameters. The *b* value can be obtained from the slope of log (i_p) *versus* log (v) plot. The *b* value determines the kinetic mechanism, where $b = 1$ indicates fast kinetic or redox reactions that occur near the surface. Under this condition, the active material exhibits a surface-controlled reaction or capacitive behaviour. In contrast, if $b = 0.5$, the active material shows a diffusion-controlled reaction or battery-like behaviour. Moreover, a transition behaviour occurs when both reactions contribute to the charge storage mechanism, and the *b* value is between 0.5 to 1. The calculated *b* values of E-NiCo-TEP-600, B-NiCo-TEP-600, and W-NiCo-TEP-600 are 0.58, 0.55, and 0.71, respectively. As the *b* values of E-NiCo-TEP-600 and B-NiCo-TEP-600 are closer to 0.5, they exhibit a battery-like behaviour with a diffusion-controlled reaction mainly contributing to the electrochemical reaction, while in W-NiCo-TEP-600, both diffusion-controlled reaction and capacitive behaviour contribute to the charge storage mechanism. To confirm this, the Dunn method (Eqs. (8) and (9)) was used to calculate the contribution of diffusion and capacitive control mechanism from CV measurements at slow scan rates.[70] In this case, the CV measurements were carried out for each sample at varying scan rates from 0.5 to 5 mV s^{-1}, as depicted in **Fig. S10a-c**.

$$I = I_{capacitive} + I_{diffusion} \quad (8)$$

$$I\,(\mathrm{V}) = k_1 v + k_2 v^{\frac{1}{2}} \quad (9)$$

$$I\,(\mathrm{V}) / v^{\frac{1}{2}} = k_1 v^{\frac{1}{2}} + k_2 \quad (10)$$

By plotting $I/v^{1/2}$ vs. $v^{1/2}$ at different potentials, we can calculate the values of k_1 (slope) and k_2 (intercept) from the linear plot. This in turn, enables us to quantify the fraction of the current at specific potentials to the capacitive effect and diffusion-controlled reaction.[71, 72] As shown in **Fig. S10d-f**, the diffusion-controlled reaction is the dominant charge storage mechanism in E-NiCo-TEP-600 and B-NiCo-TEP-600 at scan rates of 0.5 to 5 mV s^{-1}, while a more balanced contribution is observed for W-NiCo-TEP-600.

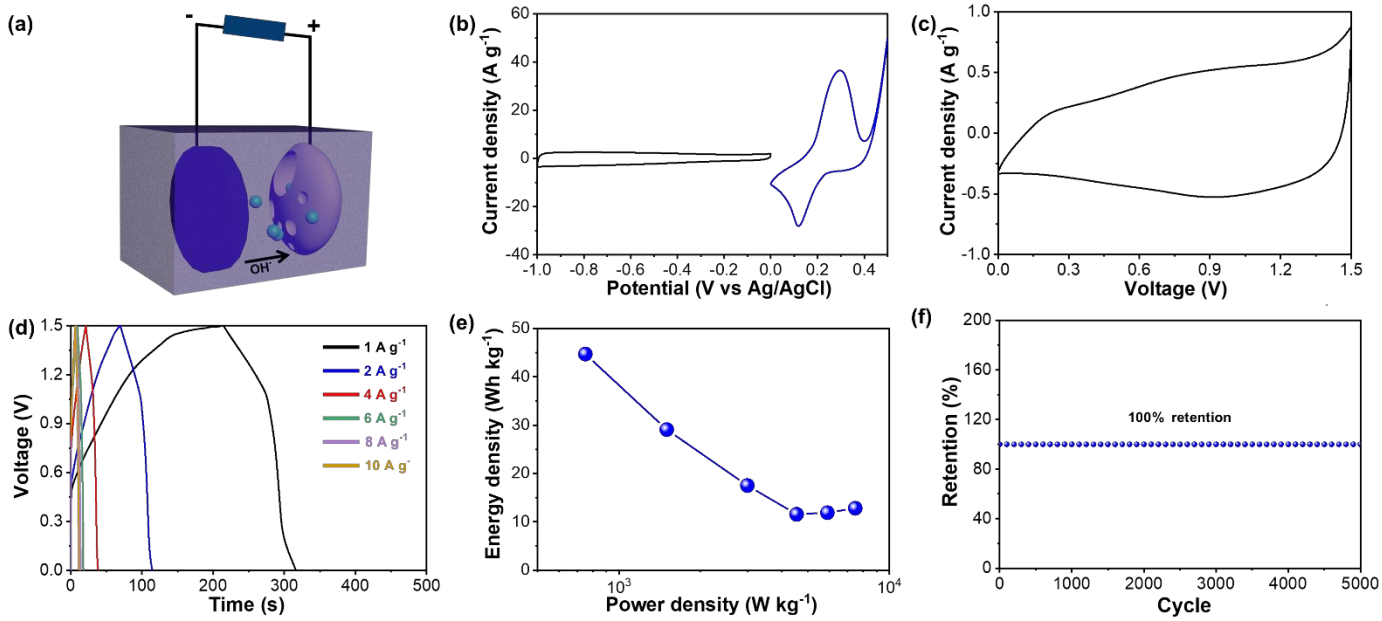

Fig. 8. (a) Illustration of the as-prepared E-NiCo-TEP-600//AC ASC. (b) CV profiles of AC and E-NiCo-TEP-600 at a scan rate of 10 mV s^{-1}. (c) CV profile of the E-NiCo-TEP-600//AC ASC at a scan rate of 10 mV s^{-1} in the potential range of 0-1.5 V. (d) GCD profile of the E-NiCo-TEP-600//AC ASC at various current densities. (e) Ragone plot of the E-NiCo-TEP-600//AC ASC. (f) Stability test of the E-NiCo-TEP-600//AC ASC for 5000 cycles at a high current density of 10 A g^{-1}.

To further demonstrate the practicality, an asymmetric supercapacitor (ASC) was fabricated using commercial AC as the anode and E-NiCo-TEP-600 as the cathode, as illustrated in **Fig. 8a**. **Fig. 8b** shows a comparison of the CV profile of commercial AC with that of E-NiCo-TEP-600 in the same three-electrode system. The CV profile of commercial AC exhibits a rectangular shape, indicating the EDLC behaviour. A potential window of 0-1.5 V vs. Ag/AgCl is chosen to check the electrochemical performance of the fabricated ASC. The CV profile of the E-NiCo-TEP-600//AC ASC is shown in **Fig. 8c**, revealing a combination of battery-like and EDLC behaviours. The specific capacitance values of this ASC were measured by GCD measurements at various current densities from 1 to 10 A g^{-1}. The E-NiCo-TEP-600//AC ASC exhibits specific capacitances of 143, 93.0, 56.0, 37.0, 38.0, and 41 F g^{-1} at current densities of 0.5, 1, 2, 4, 6, 8, and 10 A g^{-1}, respectively (**Fig. 8d**). The Ragone plot in **Fig. 8e** reveals that the E-NiCo-TEP-600//AC ASC possesses energy densities of 45, 29, and 18 Wh kg^{-1} at power densities of 750, 1504, and 2988 W kg^{-1}, respectively. The performance of this ASC is comparable to other reported metal phosphate-based ASCs, such

as $Co_3(PO_4)_2 \cdot 8H_2O$//AC (24.9 Wh kg^{-1} at 2.63 kW kg^{-1})[73], CNPO-40//BPO (36.8 Wh kg^{-1} at 254.52 W kg^{-1})[74], nickel phosphate//reduced graphene oxide (40.4 Wh kg^{-1} at 1689 W kg^{-1})[75], Ni-CPH//AC (23.4 Wh kg^{-1} at 2103 W kg^{-1})[76], and SDBS-$Ni_2Co_1PO_4$//graphene (36.5 Wh kg^{-1} at 150 W kg^{-1})[20], as depicted in **Fig. S11**. Furthermore, the stability of this ASC was tested by conducting GCD measurements for 5000 cycles at a high current density of 10 A g^{-1}. The capacitance remains highly stable after 5000 cycles, indicating the excellent stability of this ASC (**Fig. 8f**).

Table 1. Comparison of the electrochemical performance of the optimum amorphous nickel-cobalt phosphate electrode (E-NiCo-TEP-600) against previously reported metal phosphate-based electrodes.

Electrode material	Electrolyte	Potential range (V)	Current density ($A\ g^{-1}$)	Specific capacitance ($F\ g^{-1}$)	Cycling performance	Ref.
$CoPO@Fe(PO_3)_3$	3.0 M KOH	0.50	1.0	540	87.5 % after 5000 cycles at 2 A g^{-1}	55
$NiPO@Fe(PO_3)_3$	3.0 M KOH	0.50	1.0	596	90.1% after 5000 cycles at 2 A g^{-1}	55
3D flower-like cobalt phosphate	3.0 M KOH	0.50	1.0	680	89.3% after 10000 cycles at 6 A g^{-1}	56
$NaNi_{0.33}Co_{0.67}PO_4 \cdot H_2O$	1.0 M KOH	0.50	1.0	828	81.3% after 3000 cycles at 5 A g^{-1}	49
Cobalt cyclotetraphosphate ($Co_2P_4O_{12}$)	2.0 M KOH	0.50	2.5	437	100% after 300 cycles at 5 A g^{-1}	57
Cobalt manganese phosphate	1.0 M KOH	0.55	2.2	571	88% after 8000 cycles at 3 A g^{-1}	58
Flower-like superstructure of nickel metal-organic phosphate	3.0 M KOH	0.50	1.0	604	83.2% after 2000 cycles at 5 A g^{-1}	59
Nickel-copper phosphate thin film	1.0 M KOH	0.50	1.5	711	88.5% after 5000 cycles at 11.5 A g^{-1}	60
Nanotube-assembled amorphous 2D nickel phosphate	1.0 M KOH	0.50	0.5	502	94.8% after 5000 cycles at 10 A g^{-1}	19
$Co_3(PO_4)_2$ nanoflakes	3.0 M KOH	0.59	3.0	188	95% after 800 cycles at 5 A g^{-1}	61
Amorphous nickel-cobalt phosphate nanoplates (E-NiCo-TEP-600)	6.0 M KOH	0.40	2.0	1550	99% after 5000 cycles at 10 A g^{-1}	This work

4. Conclusions

In summary, we have demonstrated the fabrication of size- and shape-controlled nickel-cobalt phosphate materials from nickel-cobalt glycerate spheres. The solvent selection plays a significant role in determining the morphology of the nickel-cobalt phosphate precursor obtained from the solvothermal reaction of nickel-cobalt glycerate spheres and TEP. The use of alcohol-based solvents is found to promote the formation of plate-like particles, while the utilization of a water/ethanol mixture generates rod-like particles. Among the prepared nickel-cobalt phosphate samples, E-NiCo-TEP-600 displays the best electrochemical performance for battery-like supercapacitors with a high specific capacity of 620 C g^{-1} at 2 A g^{-1} (equivalent specific capacitance of 1550 F g^{-1}). The charge storage mechanism analysis of this electrode reveals that its charge storage mechanism is dominated by a diffusion-controlled reaction. The good electrochemical performance of E-NiCo-TEP-600 is attributed to the structural disorder and abundant defects in an amorphous material and the rich mesopores which can provide more redox sites and better pathways for ion diffusion. Furthermore, the small particle size of E-NiCo-TEP-600 can reduce the diffusion distance for electrolyte ions. The assembled E-NiCo-TEP-600//AC ASC displays a maximum energy density of 45 Wh kg^{-1} at a power density of 750 W kg^{-1}. This ASC also maintains 100% capacitance retention after 5000 cycles at 10 A g^{-1}, indicating its excellent long-term stability. The presented strategy is expected to be useful for future preparation of monodisperse amorphous metal phosphate materials for a variety of applications.

Acknowledgements

Y. V. K. acknowledges the funding from the Queensland government through the Advance Queensland Fellowship Program (AQIRF043-2020-CV). Y.Y. is grateful for the financial support given by the JST-ERATO Project (JPMJER2003) and the ES program (via Nagoya University). M. H. Y appreciated the financial support given by the National Taiwan University of Science and Technology and Bandung Institute of Technology Joint Research Program (ITB-NTUST-111-04). This work used the Queensland node of the NCRIS-enabled Australian National Fabrication Facility (ANFF).

References

1. N. Choudhary, C. Li, J. Moore, N. Nagaiah, L. Zhai, Y. Jung and J. Thomas, *Adv. Mater.*, 2017, **29**, 1605336.
2. Y. Shao, M. F. El-Kady, J. Sun, Y. Li, Q. Zhang, M. Zhu, H. Wang, B. Dunn and R. B. Kaner, *Chem. Rev.*, 2018, **118**, 9233-9280.
3. S. K. Shinde, G. S. Ghodake, N. C. Maile, H. M. Yadav, A. D. Jagadale, M. B. Jalak, A. A. Kadam, S. Ramesh, C. Bathula and D. Y. Kim, *Electrochim. Acta*, 2020, **341**, 135973.
4. J. Libich, J. Máca, J. Vondrák, O. Čech and M. Sedlaříková, *J. Energy Storage*, 2018, **17**, 224-227.
5. H. Chen, T. N. Cong, W. Yang, C. Tan, Y. Li and Y. Ding, *Prog. Nat. Sci.*, 2009, **19**, 291-312.
6. H. Gao, F. Xiao, C. B. Ching and H. Duan, *ACS Appl. Mater. Interfaces*, 2012, **4**, 2801-2810.
7. H. Wang, M. Liang, D. Duan, W. Shi, Y. Song and Z. Sun, *Chem. Eng. J.*, 2018, **350**, 523-533.
8. A. Vlad, N. Singh, J. Rolland, S. Melinte, P. M. Ajayan and J. F. Gohy, *Sci. Rep.*, 2014, **4**, 4315.
9. D.-G. Wang, Z. Liang, S. Gao, C. Qu and R. Zou, *Coord. Chem. Rev.*, 2020, **404**, 213093.
10. C. Liu, G. Xu, A. Hu, Y. Xie and H. Wang, *ChemistrySelect*, 2019, **4**, 8000-8006.
11. A. Muthuvinothini and S. Stella, *Synth. Commun.*, 2021, **51**, 2613-2627.
12. N. L. W. Septiani, Y. V. Kaneti, K. B. Fathoni, Y. Guo, Y. Ide, B. Yuliarto, X. Jiang, Nugraha, H. K. Dipojono, D. Golberg and Y. Yamauchi, *J. Mater. Chem. A*, 2020, **8**, 3035-3047.
13. N. L. W. Septiani, Y. V. Kaneti, K. B. Fathoni, K. Kani, A. E. Allah, B. Yuliarto, Nugraha, H. K. Dipojono, Z. A. Alothman, D. Golberg and Y. Yamauchi, *Chem. Mater.*, 2020, **32**, 7005-7018.
14. A. Matsuda, H. Tateno, K. Kamata and M. Hara, *Catal. Sci. Technol.*, 2021, **11**, 6987-6998.
15. M. A. Al-Omair, A. H. Touny, F. A. Al-Odail and M. M. Saleh, *Electrocatalysis*, 2017, **8**, 340-350.
16. Y. Liu, X.-J. Lin, Y.-G. Sun, Y.-S. Xu, B.-B. Chang, C.-T. Liu, A.-M. Cao and L.-J. Wan, *Small*, 2019, **15**, 1901019.
17. G. Longoni, J. K. Panda, L. Gagliani, R. Brescia, L. Manna, F. Bonaccorso and V. Pellegrini, *Nano Energy*, 2018, **51**, 656-667.
18. P. Mei, Y. V. Kaneti, M. Pramanik, T. Takei, Ö. Dag, Y. Sugahara and Y. Yamauchi, *Nano Energy*, 2018, **52**, 336-344.
19. N. L. Wulan Septiani, Y. V. Kaneti, K. B. Fathoni, J. Wang, Y. Ide, B. Yuliarto, Nugraha, H. K. Dipojono, A. K. Nanjundan, D. Golberg, Y. Bando and Y. Yamauchi, *Nano Energy*, 2020, **67**, 104270.
20. X. Zhang, N. Shang, S. Gao, C. Wang, Y. Gao and Z. Wang, *Appl. Surf. Sci.*, 2019, **483**, 529-535.
21. Y. Xi, B. Dong, Y. Dong, N. Mao, L. Ding, L. Shi, R. Gao, W. Liu, G. Su and L. Cao, *Chem. Mater.*, 2016, **28**, 1355-1362.
22. Y. Wang, W. Li, L. Zhang, X. Zhang, B. Tan, J. Hao, Z. Jian, X. Wang, Q. Hu and X. Lu, *J. Power Sources*, 2020, **449**, 227487.
23. N. Chen, J. Zhou, Q. Kang, H. Ji, G. Zhu, Y. Zhang, S. Chen, J. Chen, X. Feng and W. Hou, *J. Power Sources*, 2017, **344**, 185-194.

24. Y. V. Kaneti, R. R. Salunkhe, N. L. Wulan Septiani, C. Young, X. Jiang, Y.-B. He, Y.-M. Kang, Y. Sugahara and Y. Yamauchi, *J. Mater. Chem. A*, 2018, **6**, 5971-5983.
25. N. L. W. Septiani, Y. V. Kaneti, B. Yuliarto, Nugraha, H. K. Dipojono, T. Takei, J. You and Y. Yamauchi, *Sens. Actuators B*, 2018, **261**, 241-251.
26. L. Zhang and H. Gong, *J. Mater. Chem. A*, 2015, **3**, 7607-7615.
27. O. Gerard, A. Numan, M. A. A. M. Abdah, M. Khalid, S. Ramesh and K. Ramesh, *J. Energy Storage*, 2023, **61**, 106813.
28. N. M. Saidi, A. Khairudin, L. Li, M. A. A. M. Abdah, O. Gerard, Y. S. Tan, M. Khalid, F. Khan, M. N. Mustafa and A. Numan, *J. Energy Storage*, 2023, **73**, 108846.
29. P. Suganya, A. Venkadesh, J. Mathiyarasu and S. Radhakrishnan, *J. Solid State Chem.*, 2019, **23**, 3429-3435.
30. F. Zhang, Y. Bao, S. Ma, L. Liu and X. Shi, *J. Mater. Chem. A*, 2017, **5**, 7474-7481.
31. T. X. Nguyen, Y.-H. Su, C.-C. Lin, J. Ruan and J.-M. Ting, *Adv. Sci.*. 2021, **8**, 2002446.
32. Y. Mao, B. Zhou and S. Peng, *J. Mater. Sci: Mater. Electron.* , 2020, **31**, 9457-9467.
33. Y. Tang, Y. Liu, S. Yu, W. Guo, S. Mu, H. Wang, Y. Zhao, L. Hou, Y. Fan and F. Gao, *Electrochim. Acta*, 2015, **161**, 279-289.
34. B. Shruthi, B. J. Madhu, V. B. Raju, S. Vynatheya, B. V. Devi, G. V. Jayashree and C. R. Ravikumar, *J. Sci.: Adv. Mater. Devices*, 2017, **2**, 93-98.
35. L. George, K. Sankaran, K. S. Viswanathan and C. K. Mathews, *Appl. Spectrosc.*, 1994, **48**, 7-12.
36. P. Mäkie, P. Persson and L. Österlund, *J. Colloid Interface Sci.*, 2013, **392**, 349-358.
37. S. Rajagopalan, O. Koper, S. Decker and K. J. Klabunde, *Chem.-Euro. J.*, 2002, **8**, 2602-2607.
38. P. Mäkie, G. Westin, P. Persson and L. Österlund, *J. Phys. Chem. A*, 2011, **115**, 8948-8959.
39. E. Amaterz, A. Bouddouch, A. Tara, A. Taoufyq, Z. Anfar, B. Bakiz, L. Bazzi, A. Benlhachemi and O. Jbara, *Electrocatalysis*, 2020, **11**, 642-654.
40. C. Ruan and M. T. Rodgers, *J. Am. Chem. Soc.*, 2009, **131**, 10918-10928.
41. J. N. Kondo, K. Ito, E. Yoda, F. Wakabayashi and K. Domen, *J. Phys. Chem. B*, 2005, **109**, 10969-10972.
42. V. B. Oyeyemi, J. A. Keith and E. A. Carter, *J. Phys. Chem. A*, 2014, **118**, 3039-3050.
43. A. N. Zavilopulo, F. F. Chipev and L. M. Kokhtych, *Nucl. Inst. Methods Phys. Res.*, 2005, **233**, 302-306.
44. K. Sankaran, V. Vidya, K. S. Viswanathan, L. George and S. Singh, *J. Phys. Chem. A*, 1998, **102**, 2944-2953.
45. A. A. Mirghni, K. O. Oyedotun, B. A. Mahmoud, A. Bello, S. C. Ray and N. Manyala, *Comp. Part. B Eng.*, 2019, **174**, 106953.
46. J. Wang and H. C. Zeng, *ACS Appl. Mater. Interfaces*, 2018, **10**, 6288-6298.

47. G. F. Lenz, R. Schneider, K. M. F. Rossi de Aguiar, R. A. Bini, J. A. Chaker, P. Hammer, G. V. Botteselle, J. F. Felix and R. Schneider, *RSC Adv.*, 2019, **9**, 17157-17164.
48. Ş.-B. Ivan, I. Popescu, I. Fechete, F. Garin, V. I. Pârvulescu and I.-C. Marcu, *Catal. Sci. Technol.*, 2016, **6**, 6953-6964.
49. M. Liu, N. Shang, X. Zhang, S. Gao, C. Wang and Z. Wang, *J. Alloys Compd.*, 2019, **791**, 929-935.
50. Y. V. Kaneti, Y. Guo, N. L. W. Septiani, M. Iqbal, X. Jiang, T. Takei, B. Yuliarto, Z. A. Alothman, D. Golberg and Y. Yamauchi, *Chem. Eng. J.*, 2021, **405**, 126580.
51. L. Wan, T. Jiang, G. Ye, C. Du, M. Xie, J. Chen and Y. Zhang, *J. Alloys Compd.*, 2023, **931**, 167581.
52. H. Li, M. Zhang, X. Zhao, W. Pan and X. Sun, *J. Alloys Compd.*, 2023, **935**, 167876.
53. H. Shao, N. Padmanathan, D. McNulty, C. O'Dwyer and K. M. Razeeb, *ACS Appl. Energy Mater.*, 2019, **2**, 569-578.
54. N. O. Laschuk, E. B. Easton and O. V. Zenkina, *RSC Adv.*, 2021, **11**, 27925-27936.
55. B. Li, T. H. Meng, X. R. Meng and H. Pang, *J. Energy Storage*, 2021, **42**, 103082.
56. V. Vinothkumar, C. Koventhan, S.-M. Chen, M. Abinaya, G. Kesavan and N. Sengottuvelan, *Ceram. Int.*, 2021, **47**, 29688-29706.
57. D. R. Patil, B. Koteswararao, K. Begari, A. Yogi, M. Moussa and D. P. Dubal, *ACS Appl. Energy Mater.*, 2019, **2**, 2972-2981.
58. P. K. Katkar, S. J. Marje, V. G. Parale, C. D. Lokhande, J. L. Gunjakar, H.-H. Park and U. M. Patil, *Langmuir*, 2021, **37**, 5260-5274.
59. Y. Cheng, X. Guo, Y. Xue and H. Pang, *Appl. Mater.Today*, 2021, **23**, 101048.
60. S. S. Pujari, S. A. Kadam, Y.-R. Ma, S. B. Jadhav, S. S. Kumbhar, S. B. Bhosale, J. L. Gunjakar, C. D. Lokhande and U. M. Patil, *J. Energy Storage*, 2022, **52**, 105037.
61. J. Theerthagiri, K. Thiagarajan, B. Senthilkumar, Z. Khan, R. A. Senthil, P. Arunachalam, J. Madhavan and M. Ashokkumar, *ChemistrySelect*, 2017, **2**, 201-210.
62. M. Sohail, T. Altalhi, A. G. Al-Sehemi, T. A. Taha, K. S. El-Nasser, A. A. Al-Ghamdi, M. Boukhari, A. Palamanit, A. Hayat, M. A. Amin and W. I. Nawawi Bin Wan Ismail, *Nanomaterials*, 2021, **11**, 3245.
63. F. S. Omar, A. Numan, N. Duraisamy, S. Bashir, K. Ramesh and S. Ramesh, *RSC Adv.*, 2016, **6**, 76298-76306.
64. M. Li, M. Zhao, S. Mourdikoudis, Q. Zheng, L. Jiao, Z. Su, M. Shi, Q. Wang, Y. Wu and S. Yang, *J. Power Sources*, 2023, **580**, 233333.
65. A. M. Awwad and B. Albiss, *Adv. Mater. Lett.*, 2015, **6**, 51-54.
66. Y. Murashima, M. R. Karim, R. Furue, T. Matsui, H. Takehira, K. Wakata, K. Toda, R. Ohtani, M. Nakamura and S. Hayami, *Inorg. Chem. Front.*, 2016, **3**, 842-848.
67. C. Zhou, T. Gao, Y. Wang, Q. Liu and D. Xiao, *Appl. Surf. Sci.*, 2019, **475**, 729-739.

68. S. J. Marje, S. S. Pujari, S. A. Khalate, V. V. Patil, V. G. Parale, T. Kim, H.-H. Park, J. L. Gunjakar, C. D. Lokhande and U. M. Patil, *J. Mater. Chem. A*, 2022, **10**, 11225-11237.
69. N. K. Mishra, R. Mondal, T. Maiyalagan and P. Singh, *ACS Omega*, 2022, **7**, 1975-1987.
70. M. Salanne, B. Rotenberg, K. Naoi, K. Kaneko, P. L. Taberna, C. P. Grey, B. Dunn and P. Simon, *Nat. Energy*, 2016, **1**, 16070.
71. J. Liu, J. Wang, C. Xu, H. Jiang, C. Li, L. Zhang, J. Lin and Z. X. Shen, *Adv. Sci.*, 2018, **5**, 1700322.
72. H.-J. Zhang, Y.-K. Wang and L.-B. Kong, *Nanoscale*, 2019, **11**, 7263-7276.
73. P. K. Katkar, S. J. Marje, S. S. Pujari, S. A. Khalate, A. C. Lokhande and U. M. Patil, *ACS Sustain. Chem. Eng.*, 2019, **7**, 11205-11218.
74. D. Wang, Y. Wang, Z. Fu, Y. Xu, L.-X. Yang, F. Wang, X. Guo, W. Sun and Z.-L. Yang, *ACS Appl. Mater. Interfaces*, 2021, **13**, 34507-34517.
75. S. S. Pujari, V. V. Patil, A. S. Patil, V. G. Parale, H.-H. Park, J. L. Gunjakar, C. D. Lokhande and U. M. Patil, *Synth. Metals*, 2021, **280**, 116876.
76. B. N. Vamsi Krishna, S. Khaja Hussain and J. S. Yu, *J. Colloid Interface Sci.*, 2021, **592**, 145-155.